

# Deep HST imaging surveys and the formation of spheroidal galaxies

Giulia Rodighiero,<sup>1\*</sup> Alberto Franceschini<sup>1</sup> and Giovanni Fasano<sup>2</sup>

<sup>1</sup>*Dipartimento di Astronomia di Padova, Vicolo dell'Osservatorio, 5, I-35122 Padova, ITALY*

<sup>2</sup>*Osservatorio Astronomico di Padova, Vicolo dell'Osservatorio, 5, I-35122 Padova, ITALY*

1 February 2001

## ABSTRACT

We have extended our previous analysis of morphologically selected elliptical and S0 galaxies in the Hubble Deep Field (HDF) North to include HST data in the HDF South and the HDF-S-NICMOS areas. Our final sample amounts to 69 E/S0 galaxies with  $K < 20.15$  over an area of 11 square arcmins. Although a moderately small number over a modest sky area, this sample benefits of the best imaging and photometric data available on high-redshift galaxies. Multi-waveband photometry allows us to estimate with good accuracy the redshifts for the majority of these galaxies which lack a spectroscopic measure. We confirm our previous findings that massive E/S0s tend to disappear from flux-limited samples at  $z > 1.4$ . This adds to the evidence that the rest-frame colours and SEDs of the numerous objects found at  $0.8 < z < 1.2$  are inconsistent with a very high redshift of formation for the bulk of stars, while they are better consistent with protracted (either continuous or episodic) star-formation down to  $z \leq 1$ . These results based on high-quality imaging on a small field can be complemented with data from colour-selected Extremely Red Objects (EROs) on much larger sky areas: our claimed demise of E/S0s going from  $z = 1$  to  $z = 1.5$  is paralleled by a similarly fast decrease in the areal density of EROs when the colour limit is changed from  $(R - K) = 5$  to  $(R - K) = 6$  (corresponding to  $z \simeq 1$  and  $z \simeq 1.3$  respectively). Altogether, the redshift interval from 1 to 2 seems to correspond to a very active phase for the assembly of massive E/S0 galaxies in the field, and also probably one where a substantial fraction of their stars are formed.

**Key words:** galaxies: elliptical and lenticular, cD - galaxies: evolution - galaxies: formation - galaxies: photometry - infrared: galaxies.

## 1 INTRODUCTION

The evolution with redshift of the mass function of bright galaxies is an important discriminant among competing cosmogonic scenarios. Present instrumentation, including HST and large optical telescopes on ground, is close to provide decisive tests of these alternative schemes for galaxy formation.

The surface density of Extremely Red Objects (EROs) has been recently used by Daddi et al. (2000) to constrain the epoch of formation and the evolution of elliptical galaxies in the field. These authors claim that the density of EROs with  $(R - K) \geq 5$  (the typical colour of an old elliptical galaxy at  $z \geq 1$ ) is consistent with the passive evolution of giant ellipticals, implying an early formation of the spheroidal population through violent starbursts at high

redshifts ( $z \geq 2.5$ ). This formation paradigm for ellipticals has the nice feature to make clear and testable predictions.

On the other side, hierarchical galaxy formation models (Kauffmann & Charlot 1998) predict that elliptical galaxies form through the merging of disk galaxies at moderate redshifts. This scenario is supported by other studies emphasizing a lack of massive ellipticals at redshift greater than  $z \sim 1.5$  (Zepf 1997; Franceschini et al. 1998, hereafter FA98; Barger et al. 1999).

In particular, FA98 studied the photometric and statistical properties of a complete sample of early-type galaxies with  $K < 20.15$  in the HDF North. The FA98 sample was selected on a deep  $K$ -band image from Kitt Peak, by applying a rigorous morphological classification scheme based on the observed surface brightness profiles. FA98 found that the vast majority of bright early-type galaxies in the HDF-N are located at  $z \leq 1.3$  and display colours indicative of a fairly wide range of ages. There is a remarkable absence in the FA98 sample of objects with  $z > 1.3$ . According to the

\* E-mail:rodighiero@pd.astro.it

passive evolution scenario, these objects should be easily detected, due to the luminous star formation phase expected to happen at these redshifts.

To enforce the statistical significance of these results, an extension of the analysis to different sky regions would be critical. For this reason, we extend in this paper the study to the HDF-South WFPC2 and NICMOS fields, by selecting a new complete sample of early-type galaxies and following the same prescriptions outlined in FA98 to process the data.

For consistency with previous analyses, we assume  $H_0 = 50 \text{ Km s}^{-1} \text{ Mpc}^{-1}$  and  $q_0 = 0.15$ , with zero cosmological constant  $\Lambda$ .

## 2 SAMPLE SELECTION

The present analysis makes use of a collection of high quality, deep images, well suited for the study of field galaxies and covering three different areas: (a) the HDF-North, (b) the HDF-S WFPC2 area and the (c) HDF-S NICMOS field. Our galaxy catalog includes early-type objects selected in the near infrared in such fields.

### 2.1 Optical and near infrared imagery

We defer the reader to FA98 for details on the HDF-N observations. The WFPC2 strategy adopted for the HDF-S (Williams et al. 1998) was similar to that adopted for the HDF-N. In particular, the images were taken in the same four bands (F300W, F450W, F606W, F814W), with similar total exposure times. For each filter, several exposures, obtained in dithering mode, have been combined in a single image with pixel scale of  $\sim 0.04''$ . The sky area covered by both HDFN and HDFS is  $10.6 \text{ arcmin}^2$ .

Da Costa et al. (1998) observed the HDF-S WFPC2 area from optical to near-IR at the ESO 3.5 New Technology Telescope (NTT). The optical observations were carried out using the SUSI2 camera in binned mode, yielding a scale of  $0.16 \text{ arcsec/pixel}$ . Infrared observations were obtained in the  $J$ ,  $H$  and  $K$  bands, using the SOFI camera (scale of  $0.29 \text{ arcsec/pixel}$ ).

The HDF-S NICMOS images were acquired using camera 3 with a pixel size of  $0''.2$  and the filters F110W, F160W and F222W. The dithered images were processed, drizzled and combined giving a final pixel size of  $0''.075$  and covering an angular area of  $\sim 1 \text{ arcmin}^2$ .

The HDF-S NICMOS field has also been observed as part of the VLT-UT1 Science Verification program, using the Test Camera (VLTTTC) at the Cassegrain focus and the  $U$ ,  $B$ ,  $V$ ,  $R$ ,  $I$  filters. The total field sampled covers  $1.5 \times 1.5 \text{ arcmin}^2$  and the scale of processed images is of  $0.092 \text{ arcsec/pixel}$  (Fontana et al. 1999).

### 2.2 The photometric filter

The criteria adopted to ensure a careful selection of the sample in the HDF-N, as well as the accurate treatment of photometric data in seven passbands ( $U$ ,  $B$ ,  $V$ ,  $I$ : from HST imaging, by Williams et al. 1996;  $J$ ,  $H$ ,  $K$ : from KPNO imaging, Connolly et al. 1997) have been discussed in FA98 and Rodighiero et al. (2000). For the other fields we have

9cm!rodighiero1.ps

**Figure 1.** Histograms of the Sersic index  $n$  obtained by running GASPHOT on a crowded artificial field containing 200 toy galaxies with different magnitudes and radii. Galaxies with exponential profiles (100 objects) are binned with the solid line histogram, whereas the dotted line histogram refers to galaxies with  $r^{1/4}$  profiles.

9cm!rodighiero2.ps

**Figure 2.** Correlation between the Sersic index ( $n$ ) and the de Vaucouleurs morphological type ( $T$ ) for a sample of galaxies in the cluster Abell 2670. The morphological types were derived by visual inspection of the individual galaxies, complemented by luminosity and geometrical profiles obtained from detailed surface photometry (Fasano et al. 2001).

applied the same selection scheme used by FA98. We refer the reader to those papers for a thorough description of the procedure, while for convenience we summarize the main steps below.

#### HDF-South-WFPC2 field

Our primary selection is in the  $K$ -band, in order to minimize the biases due to the effects of  $K$  and evolutionary corrections. The sample of galaxies has been extracted from the SOFI- $K$  image, running SExtractor (Bertin & Arnouts 1996). As in FA98, to determine the limit of completeness in the  $K$  band ( $K_L$ ) for inclusion in our sample, we have used large simulated fields, including several HDF-like toy galaxies and mimicking the image quality of the  $K$ -band image. Running SExtractor on these synthetic frames allowed us to check its performance, determining the biases and the standard deviations of the magnitude estimates as a function of the surface brightness. We then derived the corrections that must be applied to the SExtractor photometry and the limit for completeness  $K_L = 20.2$  (in the standard system). From the simulations we derived also an evaluation of the  $K$ -band limiting surface brightness observable in the field,  $\mu_K \sim 23 \text{ mag/arcsec}^2$ . An analogous procedure was used to derive, for each object in the selected sample, the corrected magnitudes in the  $J$  and  $H$  bands. We did not correct optical HST magnitudes.

#### HDF-South-NICMOS field

The same procedure has been adopted for the HDF-S NICMOS field. In this case, however, we have chosen the F160W-HST band ( $\sim H$ ) for source selection, because of the higher noise in the F222W image ( $K$  band). The importance of this field concerns its depth in the near-IR (observed from the space), that allows to reach deeper limiting magnitudes. In particular, from the simulations we derived a magnitude of 22.05 for the limit of completeness in the  $H$  band. As for the HDF-S-WFPC2 field, we computed the corrections for the  $J$  and  $K$  bands, and also for the ground based observations in the  $U$ ,  $B$ ,  $V$ ,  $R$  and  $I$  bands. Note that the selection in the F160W band does not introduce appreciable bias with respect to the nominal  $K$  band selection adopted in the other fields, because the typical spectra for  $z \sim 1$  E/S0 galaxies are flat between 1.5 and 2.2 micron and are contributed by similarly old stellar populations.

## 2.3 The morphological filter

We have used the Galaxy Automatic Surface PHOTometry tool (GASPHOT; Pignatelli and Fasano 1999, 2000) to perform the morphological analysis of all galaxies brighter than the proper limiting IR-magnitudes in the WFPC2 and NICMOS fields of the HDF-S.

This tool operates on CCD images and consists of three different steps: i) first, it exploits the basic extraction capabilities of SExtractor to perform a simultaneous slicing of all selected objects with a given step of surface brightness (we used  $0^m.1$ ), providing luminosity, ellipticity and position angle profiles for each object as a function of the equivalent radius of the isophote; ii) secondly, it gives an accurate, smooth representation of the *PSF* by averaging (with a  $k$ -sigma clipping procedure) the luminosity profiles of the stars identified in the frame; iii) finally, it uses the generalized de Vaucouleurs law  $\mu_r - \mu_0 \propto (r/r_e)^{1/n}$  (where  $\mu_r$  is the surface brightness at radius  $r$  and  $r_e$  is the half light radius; Sersic 1968, see also Ciotti 1991), convolved with the proper *PSF*, to fit the equivalent luminosity profiles of galaxies, providing unbiased estimates of the profile parameters. The performances of GASPHOT are presently undergoing a systematic investigation (Pignatelli and Fasano 2001) by means of both extensive simulations of toy galaxies of different morphological types and comparison with galaxy samples whose morphology has been previously estimated by visual inspection of images and profiles. Figures 1 and 2 illustrate some preliminary results of this analysis. In particular, in Figure 1 we report the histograms of the Sersic index  $n$  obtained by running GASPHOT on a crowded artificial field containing 200 toy galaxies (with different magnitudes and radii) having exponential (100 objects) or  $r^{1/4}$  luminosity profiles. In Figure 2 we show the correlation between the Sersic index ( $n$ ) and the de Vaucouleurs morphological type (T) for a sample of galaxies in the cluster Abell 2670. In this case the morphological types were derived by visual inspection of the individual galaxies, complemented by luminosity and geometrical profiles obtained from detailed surface photometry (Fasano et al. 2001). From both the above figures the value of  $n$  given by GASPHOT appears to be a good indicator of the ‘true’ morphological type.

According to Figure 1, after running GASPHOT on our high resolution images, we decided to exclude from the final samples the galaxies with  $n \leq 2$  (considered late-type). In addition, we rejected the galaxies whose early-type classification was judged dubious at a visual inspection (3 objects in the WFPC2 field and 1 object in the NICMOS field). The final sample includes the 35 E/S0 galaxies extracted from the HDF-N in FA98, 28 galaxies from the WFPC2 field and 11 galaxies from the NICMOS field, for a total of 74 objects. Note that only 6 galaxies in the NICMOS field are brighter than the completeness limit for the WFPC2 fields ( $K_L = 20.15$ ).

In Table 1 we report the data of our sample: coordinates (at J2000), photometric redshifts and the observed  $K$  magnitudes (the data for HDFN galaxies have been published in FA98).

## 3 ANALYSIS OF THE BROAD BAND SPECTRA

### 3.1 Tools for spectral synthesis

The observed UV-optical-near/IR spectra of the sample of E/S0 galaxies presented in this work have been fitted with spectrophotometric models describing their integrated emission. In order to check the consistency of our approach, we decided to compare the results from two different codes: GRASIL (Silva et al 1998) and PEGASE (Fioc & Rocca-Volmerange 1997). As in FA98, we have considered two models describing the spectral behaviour of elliptical galaxies. We adopt a Salpeter IMF with a lower limit  $M_l = 0.15 M_\odot$  and a Schmidt-type law for the star formation rate (SFR):  $\Psi(t) = \nu M_g(t)$ , where  $\nu$  is the efficiency and  $M_g(t)$  is the residual mass of gas. A further relevant parameter is the timescale  $t_{infall}$  for the infall of primordial gas. The evolution patterns for the two models considered here are obtained with the following choices of the parameters: Model 1:  $t_{infall} = 0.1 \text{ Gyr}$ ,  $\nu = 2 \text{ Gyr}^{-2}$ ; Model 2:  $t_{infall} = 1 \text{ Gyr}$ ,  $\nu = 1.3 \text{ Gyr}^{-2}$ . The corresponding SF laws have a maximum at galactic ages of 0.3 (Mod 1) and 1.4 Gyr (Mod 2), and are truncated at 1 (Mod 1) and 3 Gyr (Mod 2) to mimic the onset of galactic winds.

A  $\chi^2$  fitting procedure has been adopted for the determination of the best solution for each galaxy spectrum. We use GRASIL as our reference model and use PEGASE only for comparison (the two give equally good fits).

### 3.2 Photometric redshifts and completeness

An application of spectrophotometric models is the determination of photometric redshifts. Our sample in the HDF-S lacks a complete spectroscopic coverage (40% of sample objects in the HDF-N have measured redshift). We deemed useful to compare the GRASIL and PEGASE redshift estimates. There is a slight tendency for GRASIL to predict larger values of  $z$ , but in general the agreement is quite good ( $\sim 10\%$ ).

The distribution in redshift of a flux limited population of galaxies provides a constraint on its evolutionary history and on the epoch of formation. However, selection effects have to be carefully taken into account, in particular the surface brightness limit, the cosmological dimming and the  $K$ -correction. Our selection in the  $K$ -band minimizes  $K$ - and evolutionary corrections as a function of redshift. Our evaluation of the effective radii allows us to control the effects of the limiting surface brightness ( $\mu_K \sim 23 \text{ mag/arcsec}^2$ ) observable in the  $K$ -band image. We found that the cutoff in surface brightness in the  $K$  image does not affect the selection above our limit of  $K_L = 20.15$ , for redshifts up to  $z \sim 2.5$ .

## 4 RESULTS AND DISCUSSION

### 4.1 Redshift distributions

Figure 3 reports the observed redshift distribution of elliptical galaxies in the HDF-S (dashed histogram), compared with that in the HDF-N (continuous line). The two distributions clearly differ: the HDF-N distribution shows a peak at

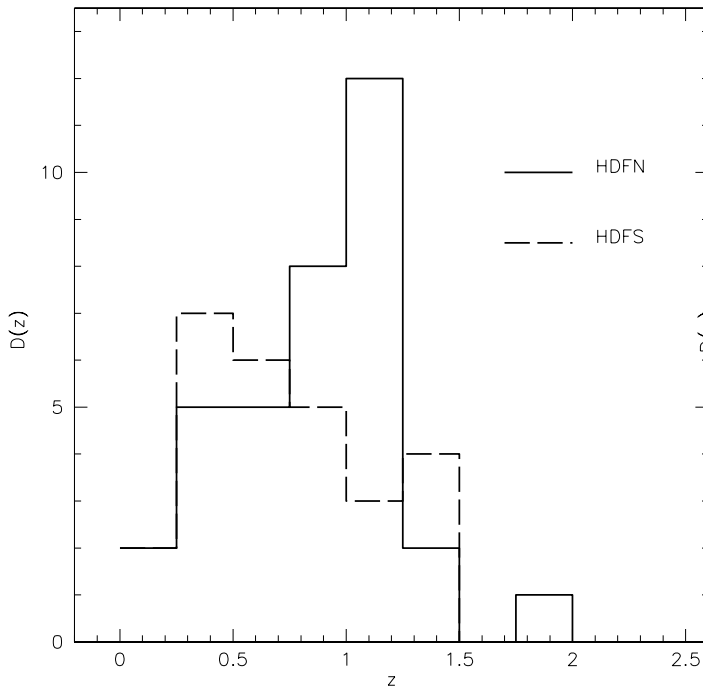


**Figure 3.** Observed redshift distribution in the HDFN (solid line) compared with that in the HDF-S (dashed line).

$z \sim 1$ , while in the HDF-S the peak is shifted toward lower redshifts ( $z \sim 0.5$ ). These differences can be explained in terms of clustering effects in the limited volumes sampled. It is worth noticing the global lack of bright spheroids in both fields at high redshifts. In particular, early-type galaxies seem to disappear at  $z \geq 1.5$ . Since this conclusion is now based on a significantly larger area than used by FA98, it is becoming more unlikely that this is due to galaxy clustering effects [see further arguments about this in Sect. 4.3].

In Figure 4 the observed distribution (continuous line) relative to the total area of  $\sim 11$  square arcminutes (HDFN + HDF-S-WFPC2 + NICMOS), for  $K < 20.15$ , is compared with the corresponding distributions predicted in the monolithic collapse scenario (dashed lines). The four panels report the predictions of Model 1 for increasing redshift of formation  $z_F$ . Low values of  $z_F$  appear to be consistent with the observed distribution ( $z_F = 1.5 \sim 2$ ), while an early epoch of formation for field E/S0 seems to be ruled out (see also Nakata et al. 1999). In particular, 39 E/S0 galaxies would be expected at  $z > 1.5$  for  $z_F = 3$  and 50 for  $z_F = 4$ , compared with the 2 observed. Our data are more consistent with the hierarchical scenario, where large galaxies are predicted to form from the merging of smaller units. This finding is in agreement with Menanteau et al. (2000), who estimate that at  $z \sim 1$  about half the field ellipticals must be undergoing episodes of star-formation.

Among the solutions proposed to explain the demise of high- $z$  ellipticals, FA98 consider the bias in the morphological filter against disturbed E/S0's (consequence of merging), which may become significant at  $z > 1$ . This point has been addressed by Rodighiero et al. (2001), who have analyzed, in a way similar to that presented in this paper, a comple-

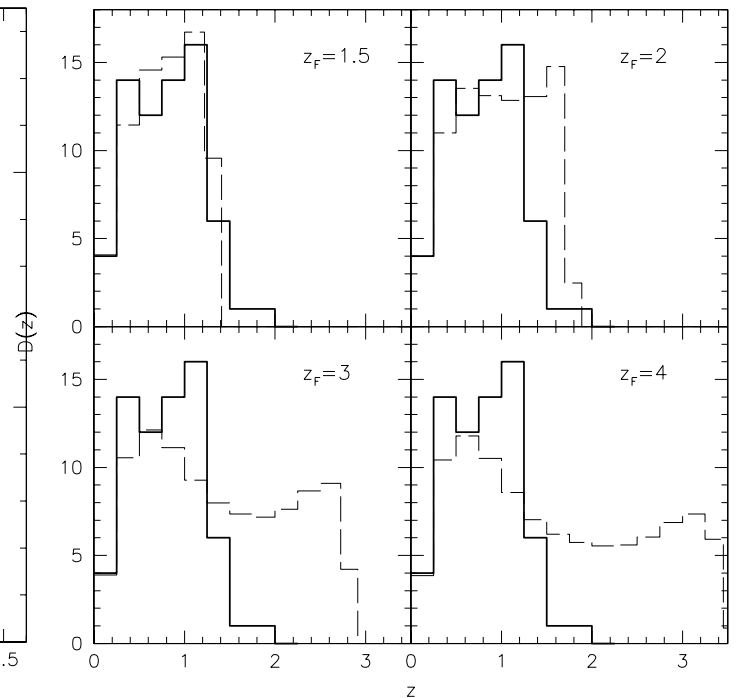


**Figure 4.** Observed total redshift distribution (solid lines), including our sample objects from the HDFN, the HDF-S and the NICMOS field at the limit magnitude of  $K_L = 20.15$ . The data are compared with predictions based on Model 1 for different redshift of formation  $z_F$  (dashed lines); from top left to down right:  $z_F = 1.5, 2, 3, 4$ .

mentary sample of 52 late-type spiral and irregular galaxies selected in the same HDF-N area with total  $K$ -magnitudes brighter than  $K=20.47$ . One of their main conclusions was about the fact that only 2 out of 52 galaxies in the sample have  $z > 1.4$ . The lack of massive galaxies of any morphological kinds at high  $z$  supports that the morphological selection of the spheroidal subsample is not responsible for its cutoff at  $z \geq 1.4$ .

## 4.2 Ages and baryonic masses for the sample galaxies

The observed galaxy SEDs present two different spectral behaviours: red objects with spectra typical of old ellipticals, and blue objects that are flatter at all wavelengths, indicating the presence of residual on-going star formation and a spread in the ages of stellar populations. Our  $\chi^2$  fitting procedure lead us to the same conclusions as found by FA98: model 2 with protracted star-formation seems to better reproduce all kinds of spectral behaviour of galaxies in the HDF-S, providing a formally acceptable total  $\chi^2$  of  $\sim 290$  (7 band data for 28 HDF-S galaxies), corresponding to a reduced chi-square of  $\chi^2_\nu \sim 1.5$ . Model 1 gives acceptable fits only for galaxies with red spectra, while the total  $\chi^2 \sim 400$  is unacceptably high ( $\chi^2_\nu \sim 2$ ). This result supports the hypothesis that, on average, star formation activity in these galaxies occurs over protracted periods (3 Gyr

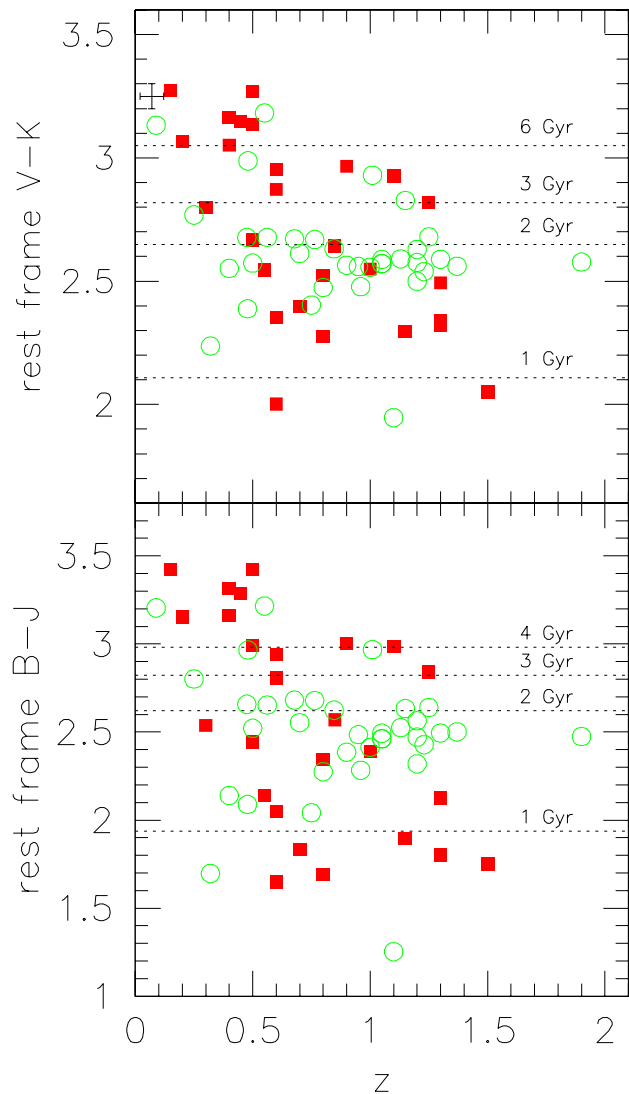


**Figure 5.** Rest frame ( $V-K$ ) (upper panel) and ( $B-J$ ) (lower panel) colours of early type field galaxies, compared with predicted values for single stellar populations with solar metallicity. Filled squares refer to HDF-S objects, open circles to the HDF-N.

in the model), rather than in short-lived single starburst (at least when considering our limited set of models).

We compare in Figure 5 the rest-frame ( $V-K$ ) and ( $B-J$ ) colours (computed from best-fitting solutions) of early-type galaxies as a function of redshift with the predicted colours of single stellar populations with solar metallicity. The colours for HDF-N ellipticals (open circles) are consistent with those found for HDF-S objects (filled squares), whereas the large spreads observed in both colour distributions correspond to a wide range of ages for the galaxies in the sample, typically from 1 to 5 Gyr. The figure shows a tendency for high redshift ellipticals to be intrinsically bluer, in particular in the HDF-S, while the clumped distribution observed in the HDF-N at  $z \sim 1$  and  $V-K \simeq 2.5$  likely indicates the presence of clustering at this redshift.

We plot in Figure 6 the baryonic masses of our sample galaxies as a function of redshift, and compare them

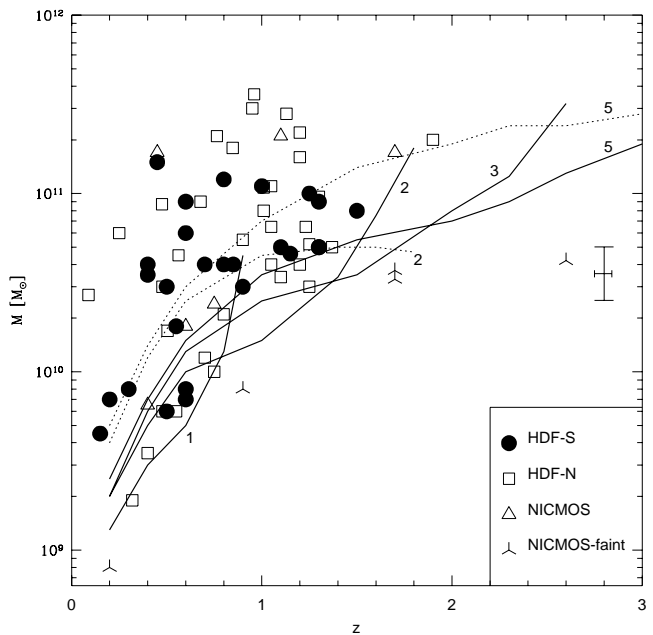


**Figure 6.** The observed baryonic mass of the sample galaxies at  $K_L = 20.15$  is plotted against the redshift. The curves represent the predictions of model 1 (dotted lines) and model 2 (solid lines) for the lowest galaxy mass still detectable within the flux limit of the survey ( $K_L = 20.15$ ) as a function of redshift for various redshift of formation (number attached to each curve). The error bar shows the mean uncertainty on the determination of the mass from spectral fitting, when considering the two different models.

with predictions of model 1 (dotted lines) and model 2 (solid lines) corresponding to the lowest galaxy mass still detectable within the flux limit of the survey ( $K_L = 20.15$ ) as a function of redshift. Different curves in the figure refer to various redshifts of formation ( $z_F$  numbers attached to each curve).

In agreement with the results of Figure 4, only low values of  $z_F$  ( $\leq 2$ ) are consistent with the observed mass distribution. In particular, the predictions of model 1 with  $z_F = 5$  are inconsistent with the observed distribution, half of the sample galaxies having estimated masses lower than the prediction. This model fails to reproduce the broad-band spectra of each single galaxy. Model 2 with  $z_F = 2$  seems to better reproduce the observations, and provides an appropriate match with the lower envelope of the mass distribution. Several galaxies at  $z < 1$  have masses requiring a lower redshift of formation ( $z_F = 1$ ).

We stress that Figure 6 does not imply that ellipticals at  $z \geq 1.5$  do not exist. Rather, according to the prescriptions of hierarchical models (Kauffmann & Charlot 1998), they are likely to be missed in our flux limited sample due to their lower mass (and luminosity). This is strongly suggested by the location in Figure 6 of the five objects selected in the NICMOS field and fainter than  $K = 20.15$  (three-pointed stars).

Benitez et al. (1999) have detected and identified in the NICMOS field 4 early-type galaxies at  $z > 1$  with  $H(AB) < 25$  (corresponding to  $H_{ST} \sim 23.6$ ). Of these, ET2 (in the Benitez et al. list) is fainter than our limit of com-

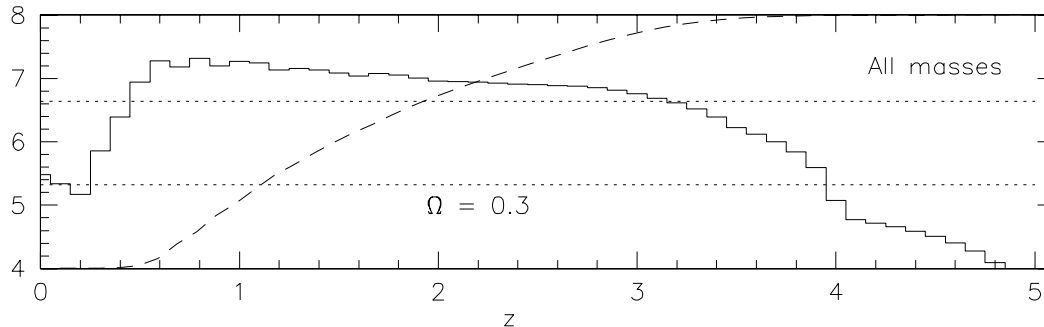


**Figure 7.** Distributions of the density of stellar mass per unit comoving volume generated in the redshift bin as a function of redshift (in  $M_{\odot} \text{ Mpc}^{-3}$  born in the redshift bin). The dashed lines represent the cumulative distributions of the mass density generated as a function of redshift, on a linear scale ranging from 0% to 100%. The dotted horizontal lines mark the 33 and 66 percentiles.

pleteness, ET1 and ET3 are included in our sample, while ET4 has been rejected as it is undetected in the VLT images and SEDs based on the NICMOS near-IR data cannot be satisfactorily fitted with any of our galaxy models.

Benitez et al. suppose that the presence of luminous red galaxies at high  $z$  in a small field indicates that evolved ( $z_F \geq 5$ ), massive galaxies are common at  $z > 1$ . They suggest that the absence of distant ellipticals claimed by others (FA98, Menanteau et al. 1999, Barger et al. 1999) may be due to the depth of the NICMOS data compared with ground-based IR data (about 3 magnitudes) or to clustering effects.

The present study is not inconsistent with the results reported by Benitez et al. First, we confirm the presence of a substantial number (21 out of 74) of E/S0 galaxies at  $z$  between 1 and 1.4. We also prove the existence of E/S0 galaxies above  $z = 1.5$ . In particular if we include the fainter NICMOS data, we find 4 early-types in NICMOS at  $1.5 < z < 3$  with  $H < 22.05$ . Our claim is rather that the baryonic masses found for these high- $z$  objects (typically few  $10^{10} M_{\odot}$  units) are typically lower than expected on consideration of the very massive ( $M > 10^{11} M_{\odot}$ ) galaxies detected around  $z = 1$  in our areas. The areal density of massive E/S0 as a function of redshift shows a drastic decrease, not a complete disappearance, above  $z \sim 1.4$ .

All this seems to favour an evolutionary scenario where the bulk of luminous spheroids are assembled at relative recent cosmic epochs ( $z_F \leq 2$ ), although not as recent as supported by Kauffmann & Charlot (1998).

Obviously, the assembly of stellar populations into the dynamically relaxed shapes of spheroids could have occurred later than the birth epochs of stars. The distribution of redshift of formation for stellar populations in E/S0 has been quantified by FA98 in their HDF-N analysis. This showed

that the bulk of stars formed at cosmic epochs between  $z = 1$  and  $z = 3$ .

The results of a similar analysis of our combined sample is reported in Figure 7. The histogram in the Figure shows the mass in stars formed per unit comoving volume in the redshift bins. This estimate is based on our best-fit photometric model solutions for all galaxies in the sample, by adding up the individual rates of star formation in the redshift bins. The mass is corrected for the portion of the luminosity function not sampled by our  $K$ -flux selection using the local observed LF in the  $K$ -band (see FA98 for details on the computation).

As shown by the figure, the history of formation of stars for this combined HDFN, HDFs, NICMOS sample is different from the partial result based on the HDF-N. The dashed curve is the normalized integral distribution: in the present case and for our adopted cosmology, 30% of stars are formed at  $z < 1$ , 40% between  $z = 1$  and 2, and the remaining 30% at  $z > 2$ .

### 4.3 Effects of cosmic variance on searches for high- $z$ spheroids

Clearly, cosmic variance affects results based on small areas such as the HDFs (see Sect. 4.1 and Figure 3). Daddi et al. (2000; hereafter DA) showed that the surface density variations of the Extremely Red Objects (EROs) population found in their survey can contribute to explain the discrepant results obtained by different authors about the density of  $z > 1$  ellipticals. Similarly, Eisenhardt et al. (2000), using a selection of  $z > 1$  elliptical galaxies based on the  $(J - K)$  colour, examined the surface density variation between their  $K$ -selected survey ( $124 \text{ arcmin}^2$ ) and the HDF-N and argued that clustering can affect results based on

small area surveys. Actually, the cosmic variance is clearly apparent in our HDF-S and HDF-N catalogues (see Figure 3, see also Lee & Hwang 2000).

Some insights about the effects of cosmic variance on our conclusions can be obtained by comparing results based on our small ( $11 \text{ arcmin}^2$ ) area with data on the surface density of EROs derived by DA for a much larger sky area ( $\sim 700 \text{ arcmin}^2$ ). DA define as EROs those objects with colours  $(R - K) \geq 5$ . They could be passively evolving galaxies at  $z > 1$  (with red colours because of the large K-correction) or heavily dust-reddened, star-forming galaxies or AGN. Using the above definition of EROs, DA found a surface density of  $0.67 \text{ EROs arcmin}^{-2}$  at the limit of their survey ( $K \leq 19.2$ ). A more stringent colour criterion of  $(R - K) \geq 6$  should select objects at  $z \geq 1.3$ . At the limit of  $(R - K) = 6$  they found a surface density of only  $0.10 \text{ EROs arcmin}^{-2}$ . If we adopt the same magnitude limit of  $K \leq 19.2$ , the corresponding surface densities for  $z > 1$  and  $z > 1.3$  ellipticals that we find in our sample are:  $0.88 \text{ arcmin}^{-2}$  ( $R - K \geq 5$ ) and  $0.17 \text{ arcmin}^{-2}$  ( $R - K \geq 6$ ). Thus, *in spite of the very different survey areas and selection criteria, the EROs statistics and our results about the fraction of E/S0 galaxies at high- $z$  turn out to be in quite good agreement. This supports our conclusions about the demise of bright massive spheroids at high redshifts.*

This fast decrease of the areal density of E/S0 at  $z > 1.5$  is likely to correspond to a fast evolution of the mass function at these epochs. Altogether, a very active phase not only for the assembly of massive E/S0 galaxies in the field but also for the origin of stellar population seems to happen around  $z \sim 1$  to  $2$ .

## 5 CONCLUSIONS

We have analyzed a  $K$ -band flux-limited sample of 69 E/S0 galaxies in three different areas (HDF-North, HDF-South and the NICMOS field, for a total of  $\sim 11 \text{ arcmin}^2$ ), where deep HST data are available. This sample is uniquely suited, as for the quality of the imaging and photometry, to the study of high-redshift spheroidal galaxies.

Our main conclusions can be summarized as follows.

- We confirm the finding by FA98 that massive E/S0s tend to disappear from flux limited samples at  $z > 1.4$ . At least the assembly of massive spheroids has to take place efficiently in the redshift interval  $1 < z < 2$ .
- The large spreads in the rest-frame colour distributions (both  $V - K$  and  $B - J$ ) for the early-type galaxies observed at  $z \sim 1$  in our sample indicate a wide range of ages, typically from 1 to 5 Gyr. These objects are inconsistent with a very high redshift of formation for the bulk of stars, and are consistent with protracted star-formation (either continuous or episodic) down to  $z \leq 1$ .
- Averaged over our (small) selected area, the bulk of stars (40%) are formed in the redshift interval  $1 < z < 2$ . Of the remaining fraction, half form at  $z < 1$  and half at  $z > 2$ .
- Our finding of a demise of E/S0s at  $z > 1.5$  in small fields is confirmed on much larger areas by a similarly fast decrease in the number density of EROs, when the

colour limits are changed from  $(R - K) > 5$  to  $(R - K) > 6$  (corresponding to an increase of the redshift cutoff from  $z \simeq 1$  to  $z \simeq 1.3$ , for typical evolved stellar spectra).

- Hierarchical models for the formation of spheroidal galaxies may naturally explain the present results.

## REFERENCES

- Barger A.J., Cowie L.L., Trentham N., Fulton E., Hu E. M., Songaila A., Hall D., 1999, AJ, 117, 102
- Benitez N., Broadhurst T., Bouwens R., Silk J., Rosati P., 1999, ApJ, 515, L65
- Bertin E., Arnouts S., 1996, A&AS, 117, 393
- Ciotti L., 1991, A&A, 249, 99
- Connolly A. J., Szalay A. S., Dickinson M., Subbarao M. U., Brunner R. J., 1997, ApJ, 486, L11
- Da Costa L., et al., 1998, astro-ph/9812105
- Daddi E., Cimatti A., Pozzetti L., Hoekstra H., Rottgering H.J.A., Renzini A., Zamorani G., Mannucci F., 2000, A&A, 361, 535 (DA)
- Eisenhardt P., Elston R., Stanford S.A., Dickinson M., Spinrad H., Stern D., Dey A., 2000, astro-ph/0002468
- Fasano, G., Bettoni, D., D'Onofrio, M., Kjærgaard, P., Moles, M., 2001, A&AS, submitted.
- Fioc M., Rocca-Volmerange B., 1997, A&A, 326, 950
- Fontana A., et al., 1999, AJ, 343, L19
- Franceschini A., Silva L., Fasano G., Granato G.L., Bressan A., Arnouts S., Danese L., 1998, ApJ, 506, 600
- Kauffmann G., Charlot S., 1998, MNRAS 297, L23
- Lee M.G., Hwang N., 2000, astro-ph/0008286
- Menanteau F., Ellis R.S., Abraham R.G., Barger A.J., Cowie L.L., 1999, MNRAS, 309, 208
- Menanteau F., Abraham R.G., Ellis R.S., 2000, astro-ph/0007114
- Nakata F., Shimasaku K., Doi M., Kashikawa N. et al, 1999, MNRAS, 309, L25
- Pignatelli, E., Fasano, G., 1999, Ap&SS 269, 657
- Pignatelli E., Fasano G., proceedings of the Granada Euroconference "The Evolution of Galaxies.I-Observational Clues", astro-ph/0009037
- Pignatelli, E., Fasano, G., 2001, in preparation
- Rodighiero G., Granato G.L., Franceschini A., Fasano G., Silva L., 2000, A&A in press, astro-ph/0010131
- Sersic J.L., 1968, Atlas de galaxias australes, Observatorio Astronomico, Cordoba
- Silva L., Granato G.L., Bressan A., Danese L., 1998, ApJ, 509, 103
- Willians R.E., et al., 1996, AJ, 112, 1335
- Willians R.E., et al., 1998, AAS, 193, 75.01
- Zepf S., 1997, Nature, 390, 377

**Table 1.** Data on the sample galaxies

id	<i>R.A.</i>			<i>DEC.</i>			<i>z</i>	<i>K</i>
	<i>h</i>	<i>m</i>	<i>s</i>	<i>°</i>	<i>'</i>	<i>''</i>		
HDFS1	22	32	54.08	-60	31	42.75	0.50	19.73
HDFS2	22	32	52.23	-60	31	52.80	1.30	19.85
HDFS3	22	32	53.37	-60	32	1.27	1.30	19.59
HDFS4	22	32	50.28	-60	32	3.30	0.60	19.44
HDFS5	22	32	55.72	-60	32	11.46	0.60	18.16
HDFS6	22	32	54.78	-60	32	15.46	0.50	18.27
HDFS7	22	32	57.75	-60	32	33.01	0.55	19.23
HDFS8	22	32	50.90	-60	32	43.02	0.40	17.69
HDFS9	22	32	54.05	-60	32	51.67	0.60	19.86
HDFS10	22	32	51.66	-60	33	6.03	1.10	19.72
HDFS11	22	32	53.92	-60	33	13.40	0.20	18.28
HDFS12	22	33	1.88	-60	33	16.36	0.30	18.89
HDFS13	22	33	2.75	-60	33	22.05	0.45	16.83
HDFS14	22	32	57.04	-60	33	23.01	1.15	19.62
HDFS15	22	32	52.16	-60	33	23.88	1.30	19.91
HDFS16	22	32	53.02	-60	33	28.49	1.00	18.44
HDFS17	22	32	54.99	-60	33	29.03	1.25	19.22
HDFS18	22	32	57.09	-60	33	28.91	0.90	19.93
HDFS19	22	32	45.32	-60	33	32.51	0.15	18.44
HDFS20	22	32	52.35	-60	33	33.05	0.80	20.10
HDFS21	22	32	51.50	-60	33	37.59	0.60	18.46
HDFS22	22	33	5.10	-60	33	46.16	1.90	19.86
HDFS23	22	32	58.60	-60	33	46.56	1.60	19.56
HDFS24	22	32	46.89	-60	33	54.83	0.40	18.05
HDFS25	22	32	52.24	-60	34	2.76	0.80	19.03
HDFS26	23	32	50.95	-60	34	5.00	1.50	19.21
HDFS27	22	32	48.90	-60	34	4.79	0.85	19.14
HDFS28	22	32	56.08	-60	34	14.20	0.70	19.59
HDFS29	22	33	0.48	-60	34	17.67	0.50	19.79
NICMOS1	22	32	51.10	-60	39	9.79	1.70	19.46
NICMOS2	22	32	50.69	-60	39	9.05	2.60	21.42
NICMOS3	22	32	53.41	-60	39	1.63	0.60	19.36
NICMOS4	22	32	53.70	-60	39	4.38	1.70	20.69
NICMOS5	22	32	52.13	-60	39	3.88	1.70	20.89
NICMOS6	22	32	53.02	-60	38	54.81	0.75	19.38
NICMOS7	22	32	52.86	-60	38	37.56	0.45	17.53
NICMOS8	22	32	51.11	-60	38	40.16	0.20	20.71
NICMOS9	22	32	55.44	-60	38	32.49	1.50	18.87
NICMOS10	22	32	50.69	-60	38	30.27	1.30	20.37
NICMOS11	22	32	53.43	-60	38	20.62	0.40	19.74
NICMOS12	22	32	52.05	-60	38	18.07	0.90	20.65